ACS Photonics

Article

pubs.acs.org/journal/apchd5

Silicon-on-Glass Graphene-Functionalized Leaky Cavity Mode Nanophotonic Biosensor

Qiushi Guo,[†,‡] Hai Zhu,[†] Feng Liu,[†,§] Alexander Y. Zhu,[†] Jason C Reed,[†] Fei Yi,[†] and Ertugrul Cubukcu*[,†,‡]

[†]Department of Materials Science and Engineering and [‡]Department of Electrical and Systems Engineering, University of Pennsylvania, Philadelphia, Pennsylvania 19104, United States

[§]Department of Physics, Shanghai Normal University, Shanghai 200234, People's Republic of China

Supporting Information

ABSTRACT: Subwavelength silicon nanostructures are known to support highly localized resonant optical modes. These resonances are spectrally narrow with an electromagnetic near-field that extends significantly into the surrounding medium. Here, we demonstrate that leaky cavity mode resonances (LCMR) in periodic silicon nanowire arrays can serve as a platform for low-cost, label-free, and highly sensitive biosensing and establish a theoretical framework for the LCMR phenomenon that is consistent with experimental results. The sensors exhibit bulk refractive index sensitivities up to 213 nm/RIU. Moreover, by functionalizing the surface of silicon nanostructures with a graphene monolayer, such structures can be used to optically detect low-concentration surface adsorption events. The specific label-free detection limit using immunoglobulin G protein (IgG) is found to be on the order of 300 pM with an extracted maximum sensor resonance shift of 5.42 nm. This sensing platform holds significant promise for unraveling protein−protein interactions and offers unique opportunities for implementation of laser sensing on a single silicon photonic chip.

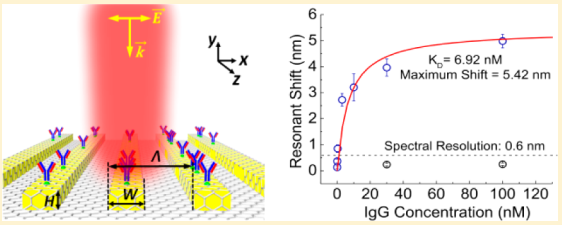

KEYWORDS: *nanophotonics, silicon nanowire, graphene, leaky cavity mode resonances, biosensor*

Nanoscale dielectric structures have recently attracted significant interest for optical waveguiding and enhanced light absorption[1−8] utilizing low loss and geometry-dependent leaky modes.[9−14] This strong Mie-like resonance results from the excitation of large displacement currents inside the dielectric cavity. They are thus ideal candidates for a broad range of applications, such as light-trapping in solar cells[15,16] and enabling optical antennas for ultracompact photodetectors.[13,17,18] In particular, owing to their small feature sizes, the fundamental resonance property of deep-subwavelength dielectric structures is leaky. This is in contrast to the interface dominated surface plasmon (SP) type effects present in their metallic counterparts.[19−24] The significant extension of the electric near-field into the bulk environment effectively associates the spectral position of the resonance to the surrounding refractive index, opening up the possibility for such structures to be used for sensing applications via time- and cost-efficient optical signal transduction methods.

Silicon is an ideal material of choice for resonant Mie cavities in the visible spectrum due to its high refractive index, relatively low intrinsic losses, and ease of integration with existing optoelectronic infrastructure. Here, we experimentally demonstrate a graphene-functionalized Si leaky cavity mode resonances (LCMR) biosensor with a label-free protein detection floor of approximately 300 pM, which is limited by spectrometer resolution. Graphene is known to possess a relatively high affinity for various biomolecules such as nucleic acids[25,26] and proteins[27,28] by virtue of $\pi-\pi$ and van der Waals interactions.[29,30] Furthermore, the atomically thin graphene exhibits low absorption in the visible,[31] preserving the excellent near-field properties and thus the sensing ability of leaky Si-based resonators. The biosensing framework eliminates the need for complicated alignment-sensitive coupling schemes, which is widely used in high quality factor dielectric microcavities, such as photonic crystals[32] and whispering gallery mode microtoroid resonators.[33] Moreover, the proposed sensor platform is fully compatible with the standard complementary metal oxide semiconductor (CMOS) fabrication process, which can enable a new generation of chip-based ultraportable bioanalysis systems.

The LCMR biosensor relies on an optical coupling scheme distinct from the leaky waveguide mode biosensor,[34] high quality factor microcavity based sensors,[32,33] and surface plasmon resonance (SPR) sensors.[35] In this scheme, normally incident light is free-space coupled to the LCMR sensor and scattered light is collected through the excitation optics similar to schemes employed for localized surface plasmon resonance (LSPR) sensors. As previously mentioned in the introduction, this eliminates the need for alignment-sensitive coupling schemes, where coupling and extraction losses on both ends

Received: October 10, 2013
Published: February 13, 2014

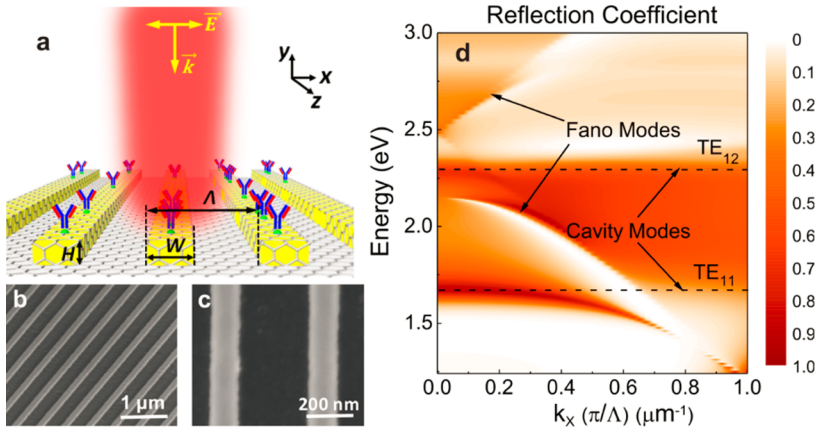

Figure 1. Overview of the LCMR sensor and its optical properties. (a) Schematic representation of a SiNW array on a glass substrate, oriented transverse to the light polarization. The graphene monolayer overlaid on the SiNW array facilitates the adsorption of various biomolecules. The array period, nanowire height, and width are denoted by Λ, *H*, and *W*, respectively. (b) SEM image of the 60° tilted SiNW array. The overall extent is 100 μm × 100 μm. (c) Magnified top view of SiNW array under SEM. The nanowires have a width of 140 nm, with a periodicity of 500 nm. (d) Photonic band diagram showing the reflection coefficient for the periodic SiNW array in the (ω, k_x) plane. The dashed lines correspond to analytically derived resonance positions for TE_{11} and TE_{12} mode. The parameters of the structure are Λ = 500 nm, *W* = *H* = 140 nm.

must be taken into account, while enabling the use of inexpensive visible optical components. Figure 1a illustrates the sensing scheme and the structure of the graphene-functionalized silicon nanowire (SiNW) LCMR biosensor. The biosensor comprises a top-down fabricated SiNW array on a glass substrate, which couples the normally incident light to LCMR modes. This resonance wavelength is strongly dependent upon the effective refractive index of the surrounding medium. Thus when biomolecules bind to the graphene/sensor surface, the effective local refractive index increases and leads to a red-shift of the LCMR, which is directly observable via far-field measurement techniques. The close-up scanning electron microscopy (SEM) images of the fabricated SiNW array are given in Figure 1b,c. The SEM images reveal the excellent uniformity in both the nanowire shape and size.

We start with a description of the resonance mechanism in arrays of SiNWs. Figure 1d shows the photonic band diagram of the structure for the *E*-field polarized along the *x* direction (TE polarization), which was calculated from the angle dependence of the optical reflection by employing the 2D transfer matrix method (the corresponding absorption band diagram is shown in Figure S1, Supporting Information). The parameters of the simulated structure are Λ = 500 nm, *W* = *H* = 140 nm. The two bands corresponding to the cavity modes are clearly visible in Figure 1d, which are flat in shape since the resonance conditions are primarily determined by the geometry of the cavity. Also present are narrow bands due to Fano or guided-mode resonances[36,37] that are sensitive to the incidence angle, with low reflection intensity under normal incidence. The excitation of the Fano mode results from the interplay between the incident light and the excited guided waves in the *x* direction.[38−42]

Analytically, since the nanowire is infinitely long but finite in *x* and *y*, the solution is two-dimensional ($\partial \mathbf{E}/\partial z = 0$): the SiNW can be considered as a two-dimensional rectangular resonator with standing waves in both *x* and *y* axes, which satisfy the requirement of momentum conservation:

$$\left(n_{Si}\frac{\omega}{c}\right)^2 = k_x^{\,2} + k_y^{\,2} \tag{1}$$

where n_{Si} is the complex refractive index of silicon and ω is the complex resonance frequency ($\omega = \mathrm{Re}(\omega) + i\mathrm{Im}(\omega)$) of the cavity. $\mathrm{Re}(\omega)$ represents the oscillation frequency of the optical field in the visible regime, and $\mathrm{Im}(\omega)$ is the attenuation due to the loss (both material and radiation). *c* is the speed of light in a vacuum, and k_x and k_y are the wavevectors in the *x* and *y* directions, respectively. The SiNW is both absorptive and radiative, giving rise to the complex solutions of $k_x = \mathrm{Re}(k_x) + i\mathrm{Im}(k_x)$ and $k_y = \mathrm{Re}(k_y) + i\mathrm{Im}(k_y)$. From the boundary conditions, the imaginary parts of the wavevectors inside nanowires enable the boundary radiation, leading to radiation loss outside, which has been termed "leaky mode resonances" in the literature.[13,16] $\mathrm{Re}(k_x)$ and $\mathrm{Re}(k_y)$ can be determined by the standing wave condition

$$\mathrm{Re}(k_x)W + 2\varphi_1 = m\pi \ (m = 1, 2, ...)$$
$$\mathrm{Re}(k_y)H + \varphi_1 + \varphi_2 = n\pi \ (n = 1, 2, ...) \tag{2}$$

where φ_1 is the reflection-associated phase shift at the interface between silicon and air, φ_2 is that between silicon and silica, and *m* and *n* are integers defining the mode orders in the *x* and *y* directions, respectively. The phase shifts of the resonances at the nanowire boundaries can be attributed to the absorptive features of SiNW in the visible light regime. It can be determined by solving the reflection coefficient *r* under normal incidence using standard Fresnel equations:

$$r_1 = |r_1|e^{i\varphi_1} = \frac{n_{Si} - 1}{n_{Si} + 1}$$
$$r_2 = |r_2|e^{i\varphi_2} = \frac{n_{Si} - n_{SiO_2}}{n_{Si} + n_{SiO_2}} \tag{3}$$

where r_1 and r_2 are the complex reflection coefficients at the Si−air and Si−SiO_2 interfaces, respectively. n_{SiO2} denotes the refractive index of glass. From the above equations, the rectangular cavity resonance position with different orders can be analytically derived. For instance, the TE_{11} cavity mode corresponds to 743 nm and the mode TE_{12} corresponds to 549 nm in the reflection spectra (dashed lines in Figure 1d), which are in good agreement with the calculated band diagram. A simulation result (Supporting Information Figure S2) demon-

dx.doi.org/10.1021/ph400073w | ACS Photonics 2014, 1, 221−227

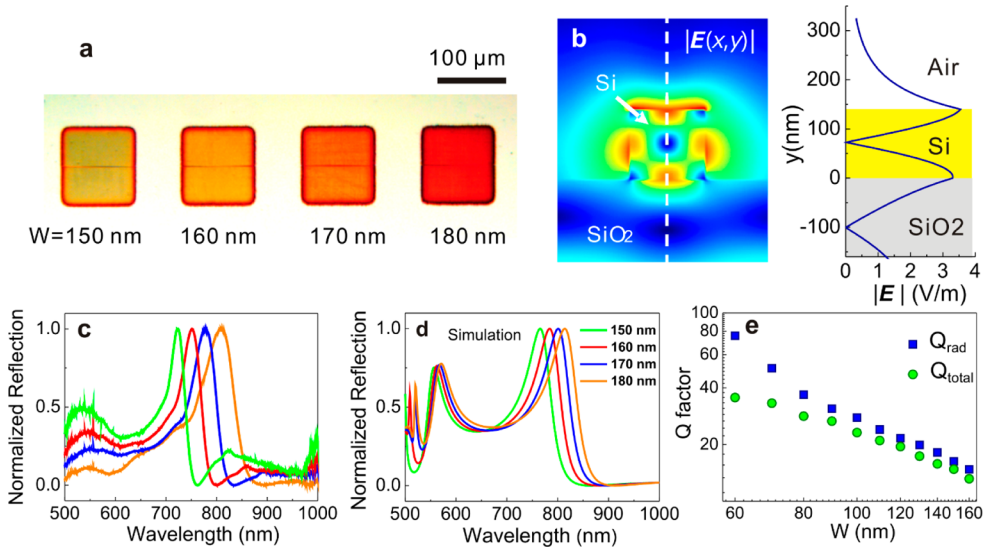

Figure 2. Size-dependent multicolor reflection of SiNW arrays. (a) Bright-field optical microscope images showing SiNW arrays of different widths and constant NW interspacing of 350 nm. (b) Simulated electric field intensity distribution of TE_{11} leaky cavity mode for a typical nanowire array with $W \times H$ = 150 nm × 140 nm, Λ = 500 nm at λ = 765 nm. The near-field distribution along the broken line in (b) illustrates the strong field localization with sufficient modal overlap with the surrounding medium. (c) Measured normalized reflection coefficient under TE incident light for representative SiNWs with W = 150 nm (green), 160 nm (red), 170 nm (blue), and 180 nm (orange). (d) Corresponding simulated reflection spectra of the same arrays. (e) FDTD-calculated total quality factor (Q_{total}) and radiation quality factor (Q_{rad}) as functions of the cavity side length W.

strates that leaky cavity modes can even be supported by a single SiNW, which has also been demonstrated by Cao et al.[43] However, employing a SiNW array greatly facilitates the measurement by increasing the reflection signal-to-background ratio.

As predicted by the above theoretical description, the LCMR wavelength can be tuned simply by changing the nanowire width and height. Tuning of leaky mode resonances with feature sizes is readily observable under an optical microscope: Figure 2a illustrates four amorphous SiNW arrays, each covering a 100 μm × 100 μm area, fabricated on a glass substrate. The nanowire widths are varied from 150 to 180 nm in steps of 10 nm. The progressive color change of SiNW arrays with varied sizes and periods can be seen in Figure 2a. At a fixed interspacing of 350 nm, a light yellow color is observed for a 150 nm SiNW array, and the color gradually changes to orange and then to red as the NW size increases to 180 nm. Through the inspection of the reflection spectra of corresponding SiNW arrays, more quantitative measurements consistent with the observed color variation are illustrated in Figure 2c. Figure 2c reveals that nanowires with widths of 150, 160, 170, and 180 nm give rise to resonance peaks at λ_0 = 722, 751, 777, and 808 nm, respectively, with an average spectral shift of 28.7 nm for each 10 nm step.

The simulated reflection spectrum, by employing the finite-difference time-domain (FDTD) method (Lumerical), is in good qualitative and reasonable quantitative agreement with the experiment in terms of the resonance position as well as the line shape, as shown in Figure 2c,d. It is worth noting that tabulated data for crystalline silicon was used in the simulation since the optical property of amorphous silicon varies greatly for different compositions. In addition, simulated spectra by incorporating the crystalline silicon data show better agreement with the experimental results (see Supporting Information Figure S3). As can be seen from Figure 2c,d, the differences in peak positions between experimental and simulation results originate from two factors. First, the fabricated silicon nanostructures are amorphous and thus have inferior optical properties than those tabulated for single-crystal materials. Second, the etched SiNW structures are not perfectly rectangular in cross-section.

As revealed by the experimental results, the LCMR are spectrally narrow (FWHM as narrow as 50−60 nm) with quality (Q) factors of 18.5 15.1, 13.9, and 11.9 for 150, 160, 170, and 180 nm nanowire arrays, respectively. It is expected that the Q factor of LCMR can be further improved by optimizing the structure since the line width of dielectric Mie resonance is strongly size dependent. In fact, low dissipation resonators with high Q factors are particularly favorable for monitoring perturbations of the resonance signal and thus for detecting biomolecules of low concentrations. It ought to be noted here that in our LMCR system with a feature size above 70 nm the dominant loss mechanism is the radiation loss of the cavity mode due to lack of total internal reflection (see Supporting Information Figure S4 and Table S1). The radiation quality factor (Q_{rad}) can be found by setting the imaginary part of the Si refractive index to be zero in computer simulations and thereby removing the intrinsic loss. Figure 2e shows the simulated radiation Q factor and total Q factor (Q_{total}) values as functions of the cavity side length W for the TE_{11} cavity mode, plotted with a logarithmic scale. Both Q_{rad} and Q_{total} increase as the cavity shrinks, but Q_{total} increases much slower since material loss becomes more pronounced for smaller resonance wavelengths. This unique behavior of Q_{rad} and Q_{total} for the 2-D leaky subwavelength cavity is significantly different from that for dielectric optical cavities with dimensions larger than the wavelength, such as in microtoroids,[44] where the total internal reflection induced Q_{rad} decreases when the cavity becomes smaller due to the larger surface curvature, leading to increased radiation leakage. Shrinking of a nanowire cross-section gives rise to larger values of stored electromagnetic energy and thus higher Q factor.[45] The easily tunable LCMR excited in deep-

dx.doi.org/10.1021/ph400073w | ACS Photonics 2014, 1, 221−227

subwavelength dielectric NW structures becomes intriguing because dielectric materials, for instance, silicon, have much lower optical losses compared to metals.

For sensing applications, the near-field confinement is the key feature. Figure 2b shows a plot of the TE_{11} total near-field profile $|E(x,y)|$ for a periodic SiNW array calculated based on the fabricated nanowire geometry assuming TE-polarized plane wave illumination with an electric field amplitude of 1 V/m. The nanowire-confined TE_{11} mode with a significant near-field intensity at the interface extends into the surrounding medium with an exponential decay constant δ_d = 62 nm (Figure 2b). The maximum electric field amplitude at the Si/air interface is 3.54 V/m. Owing to its leaky nature and spectrally sharp far-field properties, the LCMR sensor can be used to sense the refractive index changes in the surrounding environment. Figure 3 shows the responses of four SiNW arrays for a finely

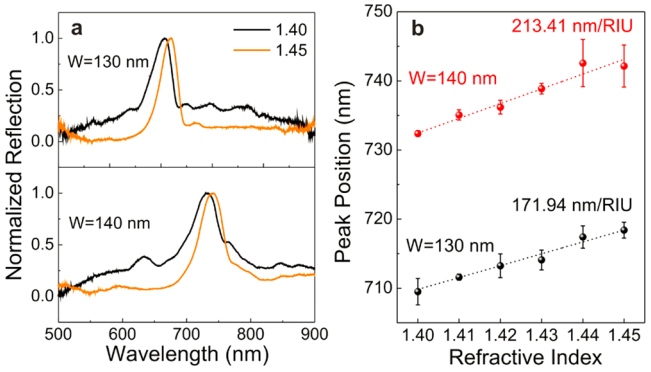

Figure 3. Experimental bulk sensitivities of the LCMR sensor over a small index range. The sensitivities of the spectral shifts ($d\lambda/dn$) for the SiNW arrays with widths of 130 and 140 nm are 171.94 and 213.41 nm/RIU, respectively. Error bars represent a standard deviation of four individual arrays with identical sizes.

controlled refractive index range (n = 1.40−1.45). Measuring the resonance peak shift as a function of the index, we determine the bulk refractive index sensitivity $d\lambda/dn$ to be as high as 213 nm/RIU, which is greater than that of localized surface plasmon resonance sensors.[46] This is as expected due to the larger field decay length δ_d (~60 nm) compared to the LSPR sensors (~20 nm). This characteristic of LCMR allows for better near-field overlap with the surrounding media. With a spectrometer-limited resolution of 0.6 nm and a sensitivity of approximately 200 nm/RIU, the minimum detectable refractive index change can be estimated as 3×10^{-3} RIU.

We also investigate the ability of the SiNW LCMR sensor to detect low-concentration label-free protein binding events. This requires the functionalization of the silicon sensor for target-receptor-type sensing as done with field-effect transistor (FET) silicon nanowire sensors.[47,48] Conventionally, Si surfaces are functionalized through a time-consuming process by introducing amino groups or carboxylic functional groups[47] such as 3-aminopropyltriethoxysilane (APTES) (9 ± 1 Å for monolayer), which is capable of vertically polymerizing in the presence of water.[49] As a result, this method potentially suffers from the disadvantages of grating efficiency degradation[50] in optical sensors and thermal instability, particularly due to the loss of covalently attached silane layers in aqueous media at 40 °C.[49] As an atomically thin, readily applicable, and stable alternative, we use a graphene monolayer overlaid on the SiNW array for sensor functionalization and promoting efficient protein adsorption. To test the efficacy of this approach, a graphene sheet grown by chemical vapor deposition[34](CVD) was mechanically transferred onto the SiNW arrays. Besides acting as a functionalization layer, the graphene monolayer is only 0.355 nm in thickness with only 2.3% absorption in the visible regime and with around 5.5% absorption further increased by the LCMR, which implies that the SiNW resonance and the corresponding optical near-fields are minimally perturbed (Supporting Information Figure S5). The quality of the transferred graphene monolayer is verified through Raman spectroscopy producing a high 2D/G peak ratio and almost negligible D peak intensity (Figure 4a).

For proximity protein sensing with the LCMR sensor we use the commercially available immunoglobulin G (IgG) antibody (Pierce). Protein A/G (Pierce), a recombinant fusion protein constituting binding domains of both protein A and protein G, was employed as the binding intermediary due to its high affinity to Fc receptors of IgG.[51,52] It effectively reduces nonspecific binding sites in the course of experiments, allowing for better sensitivity and specificity. Figure 4b shows a tilted view of a typical graphene-functionalized SiNW array after spotting 1 mg/mL A/G and 100 nM IgG. The dashed line defines the boundary between the graphene covered and bare SiNW regions. It is clearly observed that the surface density of IgG antibody attached to the graphene surface is much greater than that of the bare silicon, demonstrating the effectiveness of graphene as a protein functionalization layer. As shown in Figure 4c, the accumulated biomass on the graphene surface increases the local refractive index, resulting in a red-shift of the spectral positions of the LCMR resonances ($\Delta\lambda \approx 5$ nm after addition of 1 mg/mL protein A/G). To assess the detection limit and quantify the performance of our sensing device, IgG antibodies in 0.01 M phosphate buffer (pH = 7.4) were prepared at various concentrations. The sequentially diluted protein concentrations were verified with UV absorption spectroscopy as far as possible to ensure accurate determination of the binding affinity of IgG to our device (Supporting Information Figure S6). Each measurement was individually calibrated by calculating the relative peak shift with respect to the A/G-graphene functionalized device. Figure 4d indicates that the functional dependence of the sensor response to added protein concentration is well divided into two regimes: an initial, linear regime, where the peak shift is proportional to the concentration, and a saturation regime, where most of the binding sites are occupied by protein molecules. This is expected, since the sensing response is a surface adsorption process and can be accurately modeled by the well-known Langmuir isotherm.[53] Accordingly, we assume that the resonance peak position shift $\Delta\lambda$ is proportional to the fractional surface coverage (θ) such that $\Delta\lambda = \Delta\lambda_{max}\theta = \Delta\lambda_{max}c/(K_D + c)$. Here c is the IgG concentration (M) and $\Delta\lambda_{max}$ is the maximum LCMR shift (nm), which is proportional to the binding site surface density N ($1/m^2$) and the mode confinement factor. A lower K_D, the equilibrium dissociation constant (M), corresponds to greater binding affinity or greater adhesion strength.[54] From the fitting (solid line in Figure 4d), we determined the average equilibrium dissociation constant K_D of the IgG-A/G binding to be 6.92 nM. Error bars signify the standard deviation of four individual, identical arrays, suggesting excellent reproducibility. Given the spectrometer resolution of 0.6 nm, we find a lower detection limit of 300 pM, as shown in Figure 4 d. The fit also gives the calibrated maximum IgG sensing response $\Delta\lambda_{max}$ = 5.42 nm. The control

dx.doi.org/10.1021/ph400073w | ACS Photonics 2014, 1, 221−227

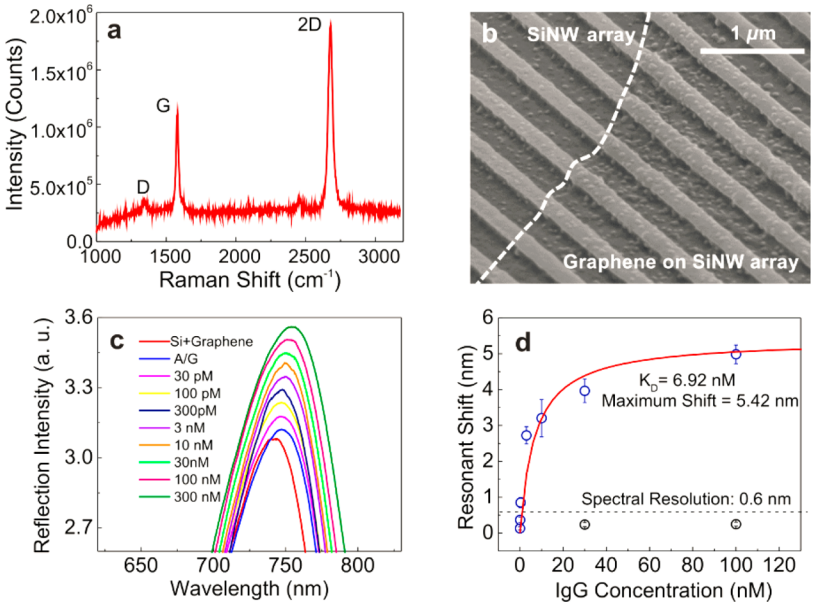

Figure 4. Demonstration of LCMR SiNW array in immunodetection. (a) Raman spectrum corresponds to the graphene-covered area. Relative intensities of the G and 2D bands suggest monolayer graphene. Absence of a significant D peak further indicates that the graphene layer is of high quality and is largely defect free. (b) SEM image of SiNW arrays after loading with 100 nM IgG protein. Dashed line sketches the boundary between the covered and noncovered areas. (c) Response of an A/G functionalized graphene covered LCMR sensor to IgG antibody with various concentrations, ranging from 30 pM to 300 nM. A/G on graphene serves as a specific binding intermediary, while IgG antibodies are the target molecules. (d) Resonant wavelength shift in response to specific binding of IgG antibody with A/G protein on graphene enabled LCMR sensor for various concentrations. The wavelength shift is taken as the value ~30 min after buffer solution wash; the red curve is fitted using the Langmuir isotherm. The error bars present standard deviation values on the mean, for multiple measurements (n = 4). Black circles below the detection limit (horizontal dashed line) show the negative control with nonspecific binding on to bare silicon surfaces.

experiments (black circles) without graphene functionalization were also carried out as shown in Figure 4d. We see the magnitude of resonant shift upon spotting of 30 and 100 nM IgG lies below the noise level, implying that a limited number of binding sites remain after the postincubation rinse. This can be understood, as bare SiNW arrays with native oxide contain silanol groups on the surface that exhibit extremely low binding affinity to biomolecules, before functionalization with amine or carboxylic groups.[47] This fact is strongly suggestive of the necessity of the graphene functionalization step in enabling the SiNWs to be used for optical biosensing purposes.

Finally, it is also important to note that there are numerous potential approaches that can further improve the detection limit as well as extend the dynamic range of our LCMR sensor. One is to use a single laser and detector sensing scheme for in situ monitoring of the reflected light intensity change in response to the changes in the bulk or local refractive index. The reflection intensity (I) sensitivity to the local refractive index (n) can be expressed as $dI/dn = dI/d\lambda \times d\lambda/dn$. For a specific resonator system, $d\lambda/dn$ is the spectral sensitivity that is determined by the magnitude of the local electric field, together with the field confinement factor of the resonator. The spectrally sharp LCMR (FWHM: 50−60 nm) in the visible region results in a very steep slope (large $|dI/d\lambda|$) around the resonance, which can, in turn, compensate for weaker field confinement and resultant spectral sensitivity (see Supporting Information Figure S7). In fact, compared to spectrometer-based sensing techniques for which the minimum detectable spectral shift is often limited by the spectral resolution of a diffractive element, a photodetector with a shot noise limited performance is expected to offer a much improved detection limit for the light intensity. By combining such an approach with active spatial modulation of the sensor with respect to the beam, even single protein level detection can be achieved through lock-in demodulation schemes by effectively removing background response, leading to very high signal-to-background levels.[55] For instance, a laser-detector implementation of the LCMR sensor compares favorably with the LSPR sensor (see Supporting Information Figure S7) while being compatible with CMOS fabrication processes, unlike the latter, which relies on gold (which acts as a contaminating dopant in the CMOS process). The integrated silicon in the LCMR can also be directly used as an on-chip photoconductive detector, circumventing the need for bulky external detectors and collection optics. In addition, by fabricating the LCMR sensor on the silicon-on-insulator platform, it is also possible to combine LCMR optical sensing with electrical sensing by using the SiNWs as a FET sensor[56] on the same chip, leading to multimodal proximity sensing.

In conclusion, the utilization of LCMR in deep-subwavelength SiNW arrays together with graphene's ability to adsorb various biomolecules results in a promising silicon-on-glass platform for future applications in on-chip photonic bioanalytics. It combines the advantages of having a compact footprint (some 100 μm × 100 μm or less), easy alignment-insensitive input−output coupling schemes, low unit cost, label-free detection, amenability for scaling up, and integration with silicon-based photonics. We have demonstrated that such low loss leaky cavity mode resonances exhibit bulk refractive index sensitivities up to 213 nm/RIU and a protein sensing limit on the order of ng/mL. For future extensions, the concept of LMCR is extremely general and can be utilized to build sensors on a wide variety of semiconductor materials and geometries. Also importantly, our proposed sensor platform is expected to

dx.doi.org/10.1021/ph400073w | ACS Photonics 2014, 1, 221−227

bring up exciting opportunities for multimodal sensing schemes.

METHODS

Electromagnetic Simulations. The optical response of SiNW array was simulated using Lumerical's FDTD Solutions. Two-dimensional models were constructed in the FDTD solver by specifying the width, thickness, periodicity, and material properties of the SiNW array. Periodic boundary conditions were imposed. We address the three-dimensional problem by targeting the two-dimensional cross-section, therefore simplifying its solution and decreasing the computational cost. A plane wave source of the appropriate bandwidth was launched toward the top of the NWs, and linear monitors were placed to collect the total reflectance as a function of wavelength.

Fabrication of SiNW Arrays. First, an amorphous silicon layer of 140 nm was deposited on a glass substrate by PECVD (Oxford PlasmaLab 100), and one ZEP 520A resist layer of ∼400 nm was spin coated onto the silicon. Then, the NW array patterns were transferred by e-beam lithography (Elionix ELS-7500EX) and developed by *O*-xylene. The ZEP 520A resist worked as the mask for the reactive ion etching process (Oxford 80 Plus) to remove part of the silicon, leaving the NW arrays. The height of the SiNW array is confirmed by atomic force microscopy.

Bulk Sensing and Spectral Measurements. Poly(dimethylsiloxane) (PDMS) fluid cells were employed as holders of refractive index matching liquids (Cargille, Series AA). In order to ensure no residual chemical remained on the sample after each trial, the samples were washed with acetone/IPA and placed under vacuum for 1 h. The reflection spectra of the nanowire arrays were taken using a homemade free-space microscope. A fiber coupled light source (Ocean Optics LS-1) was focused using a lens on the back focal plane of a 40× objective (Mitutoyo, 0.6 NA) through a 50:50 beam splitter for Kohler illumination. The light passed through the objective and uniformly illuminated the surface of the sample. The reflected light was then collected back through the same objective and a broadband polarizer and fiber-coupled into a spectrometer. All measurements were normalized to the bare glass substrate without nanowire arrays and sampled using 50 ms exposure time, 50× spectrum averaging, and 100× boxcar averaging.

Protein Preparation. In the biosensing experiment, 2 μL of protein A/G at a concentration of 1 mg/mL in PBS (0.1 M phosphate-buffered saline) was first spotted on the device surface and incubated for 1.5 h. A 30 min postincubation wash by 10 mM PBS and deionized water subsequently was carried out to remove unbound protein. Diluted IgG antibodies of varying concetrations in 10 mM phosphate buffer (pH = 7.4) were spotted on the chip surface and incubated for another 1.5 h. Finally, a second washing process (∼30 min) is performed to remove the unbound protein.

ASSOCIATED CONTENT

Supporting Information

Further details of the absorption band diagram of LCMR, LCMR in a single SiNW, simulation using amorphous silicon (n, k) data, loss mechanism of LCMR, effects of graphene monolayer coverage on LCMR, and UV quantitation of IgG sample concentrations. Additionally, the implementation of laser sensing is discussed. This information is available free of charge via the Internet at http://pubs.acs.org.

AUTHOR INFORMATION

Corresponding Author

*E-mail: cubukcu@seas.upenn.edu.

Notes

The authors declare no competing financial interest.

ACKNOWLEDGMENTS

This research was partially supported by the Partnership for Innovation program of the National Science Foundation (NSF) through grant number PFI AIR 13-12202. Part of this work is carried out at the Nano/Bio Interface Center (NSF NSEC DMR08-32802). The research of F.L. was supported by the Natural Science Foundation of China (grant no. 11104187), the China Scholarship Council (grant no. 2011831429), the Shanghai Municipal Natural Science Foundation (grant no. 11ZR1426000), and the Innovation Program of Shanghai Municipal Education Commission (grant no. 12YZ071).

REFERENCES

(1) Seo, K.; Wober, M.; Steinvurzel, P.; Schonbrun, E.; Dan, Y.; Ellenbogen, T.; Crozier, K. B. Multicolored vertical silicon nanowires. *Nano Lett.* **2011**, *11*, 1851−1856.

(2) Seo, M. K.; Yang, J. K.; Jeong, K. Y.; Park, H. G.; Qian, F.; Ee, H. S.; No, Y. S.; Lee, Y. H. Modal characteristics in a single-nanowire cavity with a triangular cross section. *Nano Lett.* **2008**, *8*, 4534−4538.

(3) Wang, B.; Leu, P. W. Tunable and selective resonant absorption in vertical nanowires. *Opt. Lett.* **2012**, *37*, 3756−3758.

(4) Aydin, K.; Ferry, V. E.; Briggs, R. M.; Atwater, H. A. Broadband polarization-independent resonant light absorption using ultrathin plasmonic super absorbers. *Nat. Commun.* **2011**, *2*, 517.

(5) Liu, N.; Mesch, M.; Weiss, T.; Hentschel, M.; Giessen, H. Infrared perfect absorber and its application as plasmonic sensor. *Nano Lett.* **2010**, *10*, 2342−2348.

(6) Wang, B.; Leu, P. W. Enhanced absorption in silicon nanocone arrays for photovoltaics. *Nanotechnology* **2012**, *23*, 194003.

(7) Zhu, J.; Yu, Z.; Burkhard, G. F.; Hsu, C.-M.; Connor, S. T.; Xu, Y.; Wang, Q.; McGehee, M.; Fan, S.; Cui, Y. Optical absorption enhancement in amorphous silicon nanowire and nanocone arrays. *Nano Lett.* **2008**, *9*, 279−282.

(8) Kuttge, M.; Garcia de Abajo, F. J.; Polman, A. Ultrasmall mode volume plasmonic nanodisk resonators. *Nano Lett.* **2010**, *10*, 1537−41.

(9) Paniagua-Domínguez, R.; Abujetas, D.; Sánchez-Gil, J. Ultra low-loss, isotropic optical negative-index metamaterial based on hybrid metal-semiconductor nanowires. *Sci. Rep.* **2013**, *3*, 1507.

(10) Coenen, T.; van de Groep, J.; Polman, A. Resonant modes of single silicon nanocavities excited by electron irradiation. *ACS Nano* **2013**, *7*, 1689−1698.

(11) Fu, Y. H.; Kuznetsov, A. I.; Miroshnichenko, A. E.; Yu, Y. F.; Luk'yanchuk, B. Directional visible light scattering by silicon nanoparticles. *Nat. Commun.* **2013**, *4*, 1527.

(12) Kuznetsov, A. I.; Miroshnichenko, A. E.; Fu, Y. H.; Zhang, J.; Luk'yanchuk, B. Magnetic light. *Sci. Rep.* **2012**, *2*, 492.

(13) Cao, L.; White, J. S.; Park, J.-S.; Schuller, J. A.; Clemens, B. M.; Brongersma, M. L. Engineering light absorption in semiconductor nanowire devices. *Nat. Mater.* **2009**, *8*, 643−647.

(14) Spinelli, P.; Verschuuren, M. A.; Polman, A. Broadband omnidirectional antireflection coating based on subwavelength surface Mie resonators. *Nat. Commun.* **2012**, *3*, 692.

(15) Yu, Y.; Ferry, V. E.; Alivisatos, A. P.; Cao, L. Dielectric core−shell optical antennas for strong solar absorption enhancement. *Nano Lett.* **2012**, *12*, 3674−3681.

(16) Cao, L.; Fan, P.; Vasudev, A. P.; White, J. S.; Yu, Z.; Cai, W.; Schuller, J. A.; Fan, S.; Brongersma, M. L. Semiconductor nanowire optical antenna solar absorbers. *Nano Lett.* **2010**, *10*, 439−445.

(17) Fan, P.; Chettiar, U. K.; Cao, L.; Afshinmanesh, F.; Engheta, N.; Brongersma, M. L. An invisible metal-semiconductor photodetector. *Nat. Photonics* **2012**, *6*, 380−385.
(18) Cao, L.; Park, J.-S.; Fan, P.; Clemens, B.; Brongersma, M. L. Resonant germanium nanoantenna photodetectors. *Nano Lett.* **2010**, *10*, 1229−1233.
(19) Barnes, W. L.; Dereux, A.; Ebbesen, T. W. Surface plasmon subwavelength optics. *Nature* **2003**, *424*, 824−830.
(20) Xia, Y.; Halas, N. J. Shape-controlled synthesis and surface plasmonic properties of metallic nanostructures. *MRS Bull.* **2005**, *30*, 338−348.
(21) Prodan, E.; Radloff, C.; Halas, N.; Nordlander, P. A hybridization model for the plasmon response of complex nanostructures. *Science* **2003**, *302*, 419−422.
(22) Lal, S.; Link, S.; Halas, N. J. Nano-optics from sensing to waveguiding. *Nat. Photonics* **2007**, *1*, 641−648.
(23) Chen, S.; Svedendahl, M.; Antosiewicz, T. J.; Käll, M. Plasmon-enhanced enzyme-linked-immunosorbent-assay on large arrays of individual particles made by electron beam lithography. *ACS Nano* **2013**, *7*, 8824−8832.
(24) Dahlin, A. B.; Wittenberg, N. J.; Höök, F.; Oh, S.-H. Promises and challenges of nanoplasmonic devices for refractometric biosensing. *Nanophotonics* **2013**, *2*, 83−101.
(25) Varghese, N.; Mogera, U.; Govindaraj, A.; Das, A.; Maiti, P. K.; Sood, A. K.; Rao, C. N. R. Binding of DNA nucleobases and nucleosides with graphene. *ChemPhysChem* **2009**, *10*, 206−210.
(26) Wang, Y.; Li, Z.; Hu, D.; Lin, C.-T.; Li, J.; Lin, Y. Aptamer/graphene oxide nanocomplex for in situ molecular probing in living cells. *J. Am. Chem. Soc.* **2010**, *132*, 9274−9276.
(27) Wan, Y.; Lin, Z.; Zhang, D.; Wang, Y.; Hou, B. Impedimetric immunosensor doped with reduced graphene sheets fabricated by controllable electrodeposition for the non-labelled detection of bacteria. *Biosens. Bioelectron.* **2011**, *26*, 1959−1964.
(28) Liu, J.; Fu, S.; Yuan, B.; Li, Y.; Deng, Z. Toward a universal "adhesive nanosheet" for the assembly of multiple nanoparticles based on a protein-induced reduction/decoration of graphene oxide. *J. Am. Chem. Soc.* **2010**, *132*, 7279−7281.
(29) Song, B.; Li, D.; Qi, W.; Elstner, M.; Fan, C.; Fang, H. Graphene on Au (111): a highly conductive material with excellent adsorption properties for high-resolution bio/nanodetection and identification. *ChemPhysChem* **2010**, *11*, 585−589.
(30) Salihoglu, O.; Balci, S.; Kocabas, C. Plasmon-polaritons on graphene-metal surface and their use in biosensors. *Appl. Phys. Lett.* **2012**, *100*, 213110−213110−5.
(31) Nair, R. R.; Blake, P.; Grigorenko, A. N.; Novoselov, K. S.; Booth, T. J.; Stauber, T.; Peres, N. M. R.; Geim, A. K. Fine structure constant defines visual transparency of graphene. *Science* **2008**, *320*, 1308.
(32) Lee, M.; Fauchet, P. M. Two-dimensional silicon photonic crystal based biosensing platform for protein detection. *Opt. Express* **2007**, *15*, 4530−4535.
(33) Armani, A. M.; Kulkarni, R. P.; Fraser, S. E.; Flagan, R. C.; Vahala, K. J. Label-free, single-molecule detection with optical microcavities. *Science* **2007**, *317*, 783−787.
(34) Zourob, M.; Simonian, A.; Wild, J.; Mohr, S.; Fan, X.; Abdulhalim, I.; Goddard, N. Optical leaky waveguide biosensors for the detection of organophosphorus pesticides. *Analyst* **2007**, *132*, 114−120.
(35) Cooper, M. A. Optical biosensors in drug discovery. *Nat. Rev. Drug Discovery* **2002**, *1*, 515−528.
(36) Fan, S.; Suh, W.; Joannopoulos, J. D. Temporal coupled-mode theory for the Fano resonance in optical resonators. *J. Opt. Soc. Am. A* **2003**, *20*, 569−572.
(37) Huang, M.; Yanik, A. A.; Chang, T.-Y.; Altug, H. Sub-wavelength nanofluidics in photonic crystal sensors. *Opt. Express* **2009**, *17*, 24224−24233.
(38) Crozier, K. B.; Lousse, V.; Kilic, O.; Kim, S.; Fan, S.; Solgaard, O. Air-bridged photonic crystal slabs at visible and near-infrared wavelengths. *Phys. Rev. B* **2006**, *73*, 115126.
(39) Ghenuche, P.; Vincent, G.; Laroche, M.; Bardou, N.; Haïdar, R.; Pelouard, J.-L.; Collin, S. Optical extinction in a single layer of nanorods. *Phys. Rev. Lett.* **2012**, 109.
(40) Yanik, A. A.; Cetin, A. E.; Huang, M.; Artar, A.; Mousavi, S. H.; Khanikaev, A.; Connor, J. H.; Shvets, G.; Altug, H. Seeing protein monolayers with naked eye through plasmonic Fano resonances. *Proc. Natl. Acad. Sci.* **2011**, *108*, 11784−11789.
(41) Cetin, A. E.; Altug, H. Fano resonant ring/disk plasmonic nanocavities on conducting substrates for advanced biosensing. *ACS Nano* **2012**, *6*, 9989−9995.
(42) Karagodsky, V.; Sedgwick, F. G.; Chang-Hasnain, C. J. Theoretical analysis of subwavelength high contrast grating reflectors. *Opt. Express* **2010**, *18*, 16973−16988.
(43) Cao, L.; Fan, P.; Barnard, E. S.; Brown, A. M.; Brongersma, M. L. Tuning the color of silicon nanostructures. *Nano Lett.* **2010**, *10*, 2649−2654.
(44) Kippenberg, T. J.; Spillane, S. M.; Vahala, K. J. Demonstration of ultra-high-Q small mode volume toroid microcavities on a chip. *Appl. Phys. Lett.* **2004**, *85*, 6113.
(45) Schuller, J. A.; Brongersma, M. L. General properties of dielectric optical antennas. *Opt. Express* **2009**, *17*, 24084−24095.
(46) Reed, J. C.; Zhu, H.; Zhu, A. Y.; Li, C.; Cubukcu, E. Graphene-enabled silver nanoantenna sensors. *Nano Lett.* **2012**, *12*, 4090−4094.
(47) Stern, E.; Klemic, J. F.; Routenberg, D. A.; Wyrembak, P. N.; Turner-Evans, D. B.; Hamilton, A. D.; LaVan, D. A.; Fahmy, T. M.; Reed, M. A. Label-free immunodetection with CMOS-compatible semiconducting nanowires. *Nature* **2007**, *445*, 519−522.
(48) Guo, Q.; Kong, T.; Su, R.; Zhang, Q.; Cheng, G. Noise spectroscopy as an equilibrium analysis tool for highly sensitive electrical biosensing. *Appl. Phys. Lett.* **2012**, *101*, 093704−093704−5.
(49) Asenath Smith, E.; Chen, W. How to prevent the loss of surface functionality derived from aminosilanes. *Langmuir* **2008**, *24*, 12405−12409.
(50) Hsiao, V. K.; Waldeisen, J. R.; Zheng, Y.; Lloyd, P. F.; Bunning, T. J.; Huang, T. J. Aminopropyltriethoxysilane (APTES)-functionalized nanoporous polymeric gratings: fabrication and application in biosensing. *J. Mater. Chem.* **2007**, *17*, 4896−4901.
(51) Berg, O. G.; von Hippel, P. H. Diffusion-controlled macromolecular interactions. *Annu. Rev. Biophys. Biophys. Chem.* **1985**, *14*, 131−158.
(52) Saha, K.; Bender, F.; Gizeli, E. Comparative study of IgG binding to proteins G and A: nonequilibrium kinetic and binding constant determination with the acoustic waveguide device. *Anal. Chem.* **2003**, *75*, 835−842.
(53) Raorane, D. A.; Lim, M. D.; Chen, F. F.; Craik, C. S.; Majumdar, A. Quantitative and label-free technique for measuring protease activity and inhibition using a microfluidic cantilever array. *Nano Lett.* **2008**, *8*, 2968−2974.
(54) Kuo, S. C.; Lauffenburger, D. A. Relationship between receptor/ligand binding affinity and adhesion strength. *Biophys. J.* **1993**, *65*, 2191−2200.
(55) Höppener, C.; Beams, R.; Novotny, L. Background suppression in near-field optical imaging. *Nano Lett.* **2009**, *9*, 903−908.
(56) Cui, Y.; Wei, Q.; Park, H.; Lieber, C. M. Nanowire nanosensors for highly sensitive and selective detection of biological and chemical species. *Science* **2001**, *293*, 1289−1292.